Electrochemical gate-controlled electron transport of redox-active single perylene bisimide molecular junctions

2008 J. Phys.: Condens. Matter 20 374122

(http://iopscience.iop.org/0953-8984/20/37/374122)

IOP PUBLISHING JOURNAL OF PHYSICS: CONDENSED MATTER

J. Phys.: Condens. Matter **20** (2008) 374122 (11pp) doi:10.1088/0953-8984/20/37/374122

Electrochemical gate-controlled electron transport of redox-active single perylene bisimide molecular junctions

C Li[1,2], A Mishchenko[1], Z Li[1], I Pobelov[1,2], Th Wandlowski[1,2], X Q Li[3], F Würthner[3], A Bagrets[4,5] and F Evers[4,5]

[1] Department für Chemie und Biochemie, Universität of Bern, CH-3012-Bern, Switzerland
[2] Institute of Bio- and Nanosystems IBN 3 and Center of Nanoelectronic Systems for Information Technology, Research Center Jülich, D-52425 Jülich, Germany
[3] Institut für Organische Chemie, Universität Würzburg, Am Hubland, 97074 Würzburg, Germany
[4] Institute of Nanotechnology, Research Center Karlsruhe, PO Box 3640, D-76021, Germany
[5] Institut für Theorie der Kondensierten Materie, Universität Karlsruhe, 76021 Karlsruhe, Germany

E-mail: thomas.wandlowski@dcb.unibe.ch, wuerthner@chemie.uni-wuerzburg.de and ferdinand.evers@int.fzk.de

Received 15 February 2008
Published 26 August 2008
Online at stacks.iop.org/JPhysCM/20/374122

Abstract

We report a scanning tunneling microscopy (STM) experiment in an electrochemical environment which studies a prototype molecular switch. The target molecules were perylene tetracarboxylic acid bisimides modified with pyridine (P-PBI) and methylthiol (T-PBI) linker groups and with bulky *tert*-butyl-phenoxy substituents in the bay area. At a fixed bias voltage, we can control the transport current through a *symmetric* molecular wire Au|P-PBI(T-PBI)|Au by variation of the electrochemical 'gate' potential. The current increases by up to two orders of magnitude. The conductances of the P-PBI junctions are typically a factor 3 larger than those of T-PBI. A theoretical analysis explains this effect as a consequence of shifting the lowest unoccupied perylene level (LUMO) in or out of the bias window when tuning the electrochemical gate potential VG. The difference in on/off ratios reflects the variation of hybridization of the LUMO with the electrode states with the anchor groups. I_T–$E_{S(T)}$ curves of *asymmetric* molecular junctions formed between a bare Au STM tip and a T-PBI (P-PBI) modified Au(111) electrode in an aqueous electrolyte exhibit a pronounced maximum in the tunneling current at −0.740, which is close to the formal potential of the surface-confined molecules. The experimental data were explained by a sequential two-step electron transfer process.

(Some figures in this article are in colour only in the electronic version)

1. Introduction

The ability to measure and control charge transport across nanometer-scale metal|molecule|metal junctions represents a key step toward the realization of molecular-based electronics [1–3]. Various experimental approaches have been employed to study molecular junctions in two- and three-terminal configurations. These include the scanning probe microscopies (scanning tunneling microscopy (STM), scanning tunneling spectroscopy (STS), conducting probe atomic force microscopy (CP-AFM)) [4–15], crossed-wire junctions [16], mechanical [17–21] and electromigration [22, 23] break junctions, nanopores [24] and mercury drop electrodes [25]. Approaches in condensed media, and in particular in an electrochemical environment, offer unique opportunities to *measure* and to *control* charge transport across single molecules [2]. The measured

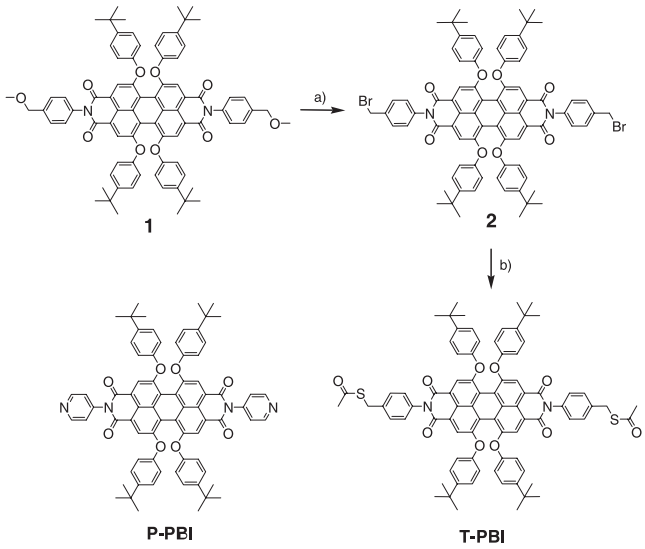

Figure 1. Chemical structures of bis-pyridyl PBI (P-PBI) and bis-thioacetyl PBI (T-PBI) and synthesis of T-PBI: (a) HBr/acetic acid, dichloromethane (DCM), argon (rt), 64 h; (b) potassium thioacetate (KSAc), N-methylpyrrolidone (NMP), argon, 60 °C, 3 h.

current represents both, the electrical contact to the external circuit and the functional state of the tailored molecule.

Employing *in situ* STM or a planar nanogap electrode configuration and the concept of '*electrolyte gating*' [14, 25–29], several groups demonstrated in the first pioneering studies transistor- and diode-like functions with high current amplification and rectification ratios [30–36]. These examples include porphyrines [14, 37], viologen-type molecular wires [31, 36, 38, 39], aniline and thiophene oligomers [30, 34, 40, 41], metal transition complexes [35, 42, 43], nitro-derivatives of oligophenylene ethynelene [44, 45] and ferrocene [46], perylene tetracarboxylic diimide [33, 47] and the redox protein azurin [32, 48]. Most of these studies refer to Au (or Pt)|molecule|Au junctions constructed in a vertical STM configuration or a planar assembly of molecular-size nanoelectrodes in an aqueous electrolyte and at ambient conditions [2, 3, 30]. Albrecht *et al* [43] introduced ionic liquids. First studies with substituted aliphatic α,ω-alkane derivatives by Higgins [49] and Chen *et al* [50], and aromatic 1,4-diaminobenzene-type molecular wires by Venkataraman *et al* [51] at solid|liquid interfaces illustrate the potential of chemical control, e.g. the effect of electron-donating (respectively-withdrawing) substituents or variable anchoring groups on the conductance signatures of single molecular junctions. However, there is still a considerable gap in our understanding of the basic relationships between molecular structures and conductance properties.

In the present study we aim to explore charge transport and switching in Au|redox molecule|Au junctions employing an electrochemical SPM-based technique [36, 52]. The target molecules chosen are pyridine (P-PBI) and thiol-terminated (T-PBI) perylene-3,4:9,10-tetracarboxylic acid bisimides (PBIs) that contain bulky *tert*-butyl-phenoxy substituents at 1,6,7,12 bay positions (figure 1). These substituents create a steric strain in the bay area leading to a propeller-like twisting of the two naphthalene half units [53, 54], which prevent π–π stacking between adjacent molecules and therefore promotes the formation of single molecule junctions. PBIs represent a unique class of n-type semiconductors [55, 56] with applications to organic or polymer light-emitting diodes [57], organic field effect transistors [58] or solar cells [59]. The highest occupied (HOMO) and lowest unoccupied (LUMO) orbitals of the parent PBI exhibit nodes at the positions of the imide nitrogens, providing unique opportunities for modifying the structure of the N-substituted side chains, but without alterations of the electronic properties of the core π-system. On the other hand, bay area substitution may lead to pronounced changes of the redox (respectively semiconducting) properties and of the dihedral twisting angle [54, 55, 60, 61]. This enables one to adjust the electronic properties of PBI from electron poor to electron rich without changing the size in the direction of the long molecular axis that will be used to connect these molecules to the electrodes. Voltammetric and spectro-electrochemical studies with PBI dissolved in polar organic solvents reveal two reversible one-electron reduction processes (formation of the stable radical anion $PBI^{\cdot -}$ or the dianion PBI^{2-}, respectively) and one reversible one-electron oxidation (formation of the radical cation $PBI^{\cdot +}$) process [62, 63].

This paper represents the first part of a systematic study of charge transport properties of bay area substituted PBI molecules in gold nanojunctions. We first report macroscopic electrochemical data employing cyclic voltammetry. Then we present single junction conductance experiments on P-PBI and T-PBI immobilized between a gold STM tip and a Au(111)-(1 × 1) substrate. These experimental investigations were combined with *ab initio* transport calculations to explain our experimental findings.

2. Experimental details

2.1. Synthesis

All solvents and reagents were purchased from commercial sources and used as-received without further purification. The solvents for spectroscopic studies were of spectroscopic grade and used as-received. ^{1}H nuclear magnetic resonance (NMR) and ^{13}C NMR spectra were recorded on a 400 MHz spectrometer and all the spectra were calibrated against tetramethylsilane (TMS). UV/vis spectra were measured on a Perkin-Elmer Lambda 40P spectrometer. N,N'-bis-(4-pyridyl)-1,6,7,12-tetrakis-(4-*tert*-butyl-phenoxy)-3,4:9,10-perylene bisimide (P-PBI) was synthesized according to reference [64], N,N'-bis-(4-bromomethyl-phenyl)-1,6,7,12-tetrakis-(4-*tert*-butyl-phenoxy)-3,4:9,10-perylene bisimide (**2**) was synthesized according to [65].

N,N'-bis-(4-acetylthiomethyl-phenyl)-1,6,7,12-tetrakis-(4-*tert*-butyl-phenoxy)-3,4:9,10-perylene bisimide (T-PBI): perylene bisimide **2** (43 mg), potassium thioacetate (KSAc) (9 mg) and N-methylpyrrolidone (NMP) (3 ml) were stirred at 60 °C for 3 h under an argon atmosphere. After cooling to room temperature, 100 ml 1 mol l^{-1} HCl was added to the mixture and the precipitate was collected and washed thoroughly with

water. Subsequent purification by column chromatography (dichloromethane/methanol: 50/1) afforded a dark red solid in a yield of 57%. Melting point, 378 °C; ^{1}H-NMR (400 MHz, $CDCl_3$, 300 K, TMS): $\delta = 8.23$ (s, 4H, Hpery), 7.40 (d, 4H, $J = 8.4$ Hz, Ar–H), 7.23 (m, 8H, Ar–H), 7.17 (d, $J = 8.4$ Hz, 4H, Ar–H), 6.85 (m, 8H, Ar–H), 4.16 (s, 4H, –CH_2–S), 2.35 (s, 6H, CO–CH_3), 1.26 (s, 36H, CH_3). ^{13}C-NMR (100 MHz, $CDCl_3$, 300 K, TMS): 194.9, 163.5, 156.1, 152.8, 147.4, 138.2, 134.1, 133.1, 129.8, 128.7, 126.6, 122.5, 120.7, 120.5, 119.7, 119.3, 34.3, 33.0, 31.4, 30.3; MS (matrix-assisted laser desorption/ionization time-of flight (MALDI-TOF), matrix DCTB): calculated for $C_{82}H_{74}N_2O_{10}S_2$: 1310.478, found 1310.480. UV/vis (CH_2Cl_2): $\lambda_{max}(\varepsilon) = 453$ (40 500), 541 (35 800), 581 (58 600 l mol^{-1} cm^{-1}).

2.2. Electrochemical studies

2.2.1. Electrolyte solutions, electrodes and voltammetric measurements. The electrolyte solutions were prepared from Milli-Q water (10 MΩ, 2 ppb total organic carbon), $LiClO_4$ (Merck, Suprapure), NaOH (Merck, Suprapure), or dichloromethane (DCM, Acros, HPLC grade) and $TBAPF_6$ (Fluka, electrochemical grade). All electrolytes were deaerated in argon (5 N) before and during the experiments. The measurements were carried out at 25 ± 0.5 °C. The glassware was cleaned in caroic acid followed by extended rinsing with Milli-Q water.

Single crystal Au(111) electrodes were cylinders (electrochemistry, 4 mm high and 4 mm diameter) or discs (STM, 2 mm high and 10 mm diameter). They were flame-annealed with a hydrogen torch at red heat, and then cooled in high purity argon. Contact with the electrolyte was always established under potential control.

The macroscopic electrochemical measurements were carried out with a lab-built potentiostat [66]. A platinum wire and a Ag/AgOx wire served as counter (respective reference) electrodes in experiments with DCM. The stability of the reference electrode was checked with ferrocenemethanol. A platinum wire and a trapped hydrogen electrode served as counter and reference electrodes in all experiments in aqueous electrolytes. Finally, we converted the potential scale with reference to a saturated calomel electrode (SCE).

2.2.2. Electrode modification. The P-PBI and T-PBI adlayers were prepared by immersion of a freshly flame-annealed unreconstructed Au(111)-(1 × 1) single crystal into a 10 mM solution of deoxygenated DCM at 20 °C. The exposure time for P-PBI was 2 min, followed by 20 s rinsing in isopropanol and Milli-Q water. In the case of T-PBI we carried out the assembly in a deoxygenated container filled with 10 μM solution in DCM, typically for 12 h at 20 °C. The T-PBI coverage could be controlled by tuning the assembly time and temperature.

2.2.3. STM and STS measurements. The STM and STS experiments (current–distance, current–voltage characteristics) were carried out with a modified Pico-SPM (Molecular Imaging Corporation) equipped with a custom-designed dual feedback preamplifier control circuit [52, 66]. The set-up is capable of measuring currents between 1 pA and 160 μA with high accuracy and dynamics. The data were recorded with a Yokogawa DL 750 multi-channel digital oscilloscope (1 M s^{-1}, 16 bit).

All experiments were carried out in a sealed, argon-filled chamber to prevent oxygen exposure under strict electrochemical potential control. The STM tips were electrochemically etched gold wires (0.25 mm diameter) coated with polyethylene. The leakage current was typically less than 1 pA. Two platinum wires served as reference and counter electrodes, respectively. All experiments were carried out in an aqueous electrolyte (0.05 M $LiClO_4$, pH 12) with no PBI derivatives present in the bulk electrolyte.

Single molecular conductance characteristics (i_T–Δz) were obtained by the repeated formation and breaking of molecular junctions formed between a Au STM tip and an adsorbate-covered substrate [52]. The following sequence was applied: a sharp gold STM tip, usable for imaging experiments with atomic resolution, was brought to a preset tunneling position, typically defined by $i_T = 50$ or 100 pA and E_{bias} ranging between ±0.050 V and ±0.300 V. Subsequently, the STM feedback was switched off, and the tip approached the PBI-modified substrate surface at constant x–y position until a preset current (5–20 μA) was reached. These settings ensured a rather strong interaction between the Au tip and the P-PBI (respectively T-PBI) adlayers. After a duration of 100 ms, the tip was retracted at a rate of 4–8 nm s^{-1} until a lower limiting current was reached ensuring all previously formed molecular junctions were broken. The cycle was repeated 2000–3000 times to provide a sufficient data base for the statistical analysis.

The retraction or pulling i_T–Δz curves were typically recorded at 1 pA $\leqslant i_T \leqslant$ 100 nA. We observed three types of transient curves. Type I curves (70%) are exponential and represent direct tunneling between the Au tip and the substrate without molecular junctions being formed. Type II curves (15%) are non-monotonic and noisy, which could be attributed to mechanical, thermal and tip instabilities. Traces of type I and II were rejected in the further analysis of the experimental data. The remaining type III conductance traces exhibit characteristic single plateaus (dominant) or series of plateaus separated by current steps. These steps are assigned to the breaking of individual (respectively multi-molecular) junctions of the PBI derivatives previously formed between the Au STM tip and the substrate surface.

Our experimental technique is distinctly different from the original approaches reported by Xu *et al* [13] and Haiss *et al* [31]. The choice of the dual preamplifier stage enabled us to separate tip distance control and recording of the transport characteristics, which leads to a significantly improved stability and reproducibility of the experiment.

The statistical analysis of the i_T–Δz traces was performed by constructing plateau-counting histograms (selection criteria: minimum plateau length 0.04 nm, average variation of the current magnitude <5%) or all data-point histograms (summing up of all data points in a predefined bin size). Further

technical details of our data analysis were described in a recent paper [52].

Complementary current–voltage experiments (i_T–$E_{S(T)}$ at fixed bias voltage $E_{bias} = E_T - E_S$) were carried out to explore the tunneling characteristics of asymmetric tunneling junctions. An adsorbate-free STM tip was stabilized above the modified substrate in the tunneling regime at a predefined x–y–z position, typically at $i_T = 100$ pA and $E_{bias} = 0.10$ V in the stability region of the uncharged PBI. Subsequently, the z-piezo feedback was switched off, and several i_T–$E_{S(T)}$ traces were recorded at fixed bias by simultaneously ramping the potentials of tip and substrate with 0.5 or 1.0 V s^{-1}. We recorded individual scans with 1000 data points. The cycle was repeated after stabilization at a preset value of i_0. The data presented in this paper are the average of ten individual traces.

The recording of individual i_T–Δz and i_T–$E_{S(T)}$ traces was alternated with monitoring *in situ* STM images (using the same Au tip!) and cyclic voltammograms to ensure that substrate, adlayer and tip remained intact.

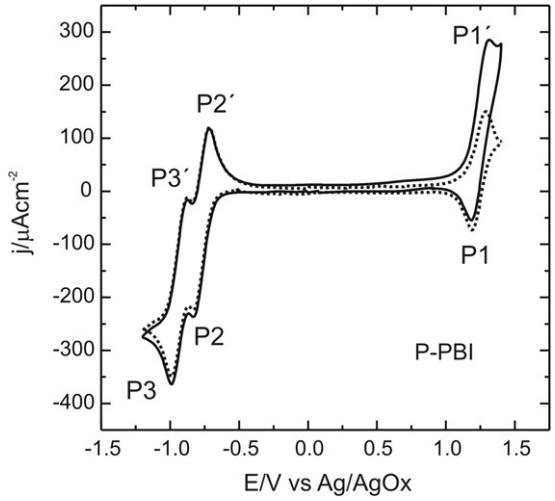

Figure 2. Cyclic voltammograms of 1 mM N-PBI in CH_2Cl_2 + 0.1 M $TBAPF_6$ recorded with a Au(111) electrode (solid line) at a scan rate of 0.1 V s^{-1}. The dotted line represents the curve after baseline correction.

3. Results and discussion

3.1. Cyclic voltammetry of PBI derivatives in DCE

Figure 2 shows a typical cyclic voltammogram of 1 mM P-PBI in DCM with 0.1 M $TBAPF_6$ as the supporting electrolyte. One may distinguish three characteristic pairs of current peaks labeled P1|P1′, P2|P2′ and P3|P3′. The positions of the characteristic potentials are independent of scan rate v in 0.01 V s^{-1} $\leqslant v <$ 1.00 V s^{-1}, and the peak heights scale linearly with $\sqrt{v}$ (after careful baseline correction), indicating reversible, bulk-diffusion controlled processes. The peak-to-peak separation of P1|P1′ is estimated to be 0.065 ± 0.010 V, which suggests a one-electron process. However, extended long-time excursion into the potential region $E > 0.50$ V indicates a slow decomposition of P-PBI accompanied by the formation of a blocking adlayer. The peak-to-peak separations between P2|P2′ and P3|P3′ are also independent of scan rate and amount to 0.125 ± 0.010 V and 0.110 ± 0.020 V, in agreement with literature data [55, 62, 63]. These values are larger than those expected for an ideal one-electron process. Clearly, the interfacial reaction is more complex. Mechanistic details are not yet understood.

Comparing our observations with results reported in the literature [55, 62, 63] we assign P1|P1′ to the reversible one-electron oxidation P-PBI|P-PBI$^{\cdot+}$ and P2|P2′ (respectively P3|P3′) to two one-electron reduction processes P-PBI|P-PBI$^{\cdot-}$ and P-PBI$^{\cdot-}$|P-PBI^{2-}, the latter generating the radical anion P-PBI$^{\cdot-}$ (respectively the dianion PBI^{2-}). The electron-donating 4-*tert*-butyl-phenoxy substituents shift the reduction processes 0.100 V towards negative potentials and the oxidation 0.300 V towards negative values, compared to the unsubstituted parent molecule PBI [73].

Similar processes are expected for T-PBI. However, the electrochemistry characteristics of the bulk solution are distorted by the chemisorption of the molecule on the Au working electrode via the thiol linker group.

We have performed *ab initio* calculations based on density functional theory to reveal details of the 'reductive charging' process using the standard quantum chemistry package TURBOMOLE [67]. We considered an '*extended molecule*' composed of the PBI derivative bridged between two pyramids of ∼40 Au atoms with the experimental lattice constant (4.08 Å) modeling the Au electrodes. We employed the generalized gradient approximation (GGA; BP86 functional [68]) with a fully atom optimized, contracted Gaussian-type basis set with SVP quality (split valence basis including polarization functions) [69].

We find that the LUMO, which accepts the first electron, extends over the entire perylene unit in both cases, P-PBI and T-PBI, and hybridizes only weakly with the lead orbitals. Since these calculations also show that the neighboring orbitals (HOMO and LUMO + 1) are separated by $\Delta = 1$–2 eV in energy, we expect that our theoretical findings remain valid in an electrochemical environment even though the present calculation does not take the effects of the solvent into account. Within this picture, an explanation is readily obtained for the closeness of the two redox peaks, P2|P2′ and P3|P3′ observed experimentally in figure 2. The Coulomb interaction between two extended orbitals is $U \approx e^2/\varepsilon R$, where ε is the dielectric constant of the embedding medium (for DCM $\varepsilon \approx 10\varepsilon_0$ and for water $\varepsilon \approx 80\varepsilon_0$) and R is the typical size of the molecular orbital ($R \approx 10$ Bohr radii). Inserting numbers, we have $U \ll \Delta$, so that the additional energy cost for a double occupancy is quite small.

3.2. Cyclic voltammetry with surface-immobilized adlayers

P-PBI and T-PBI were immobilized on Au(111)-(1 × 1) electrodes following the protocols outlined in section 2.2. STM images recorded *ex situ* and *in situ* (in an aqueous electrolyte) indicate that the T-PBI and P-PBI adlayers, independent of assembly time or temperature, are rather disordered. No long-range order was observed. The coverage could be tuned by changing the perylene concentration in the assembly solution and/or the exposure time.

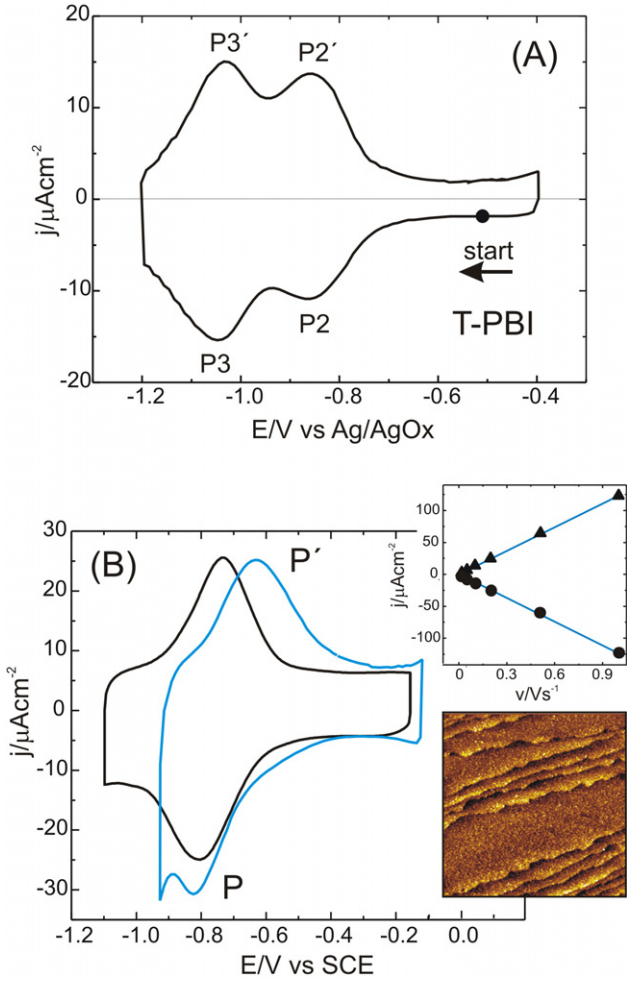

Figure 3. (A) Cyclic voltammograms of a monolayer of T-PBI immobilized on Au(111)-(1 × 1) in $CH_2Cl_2 + 0.1$ M $TBAPF_6$, scan rate 0.2 V s^{-1}. (B) Cyclic voltammograms of T-PBI (black solid line) and P-PBI (blue solid line) immobilized on Au(111)-(1 × 1) in aqueous 0.05 M $LiClO_4$, pH ∼ 12, scan rate 0.2 V s^{-1}. The insets show the scan rate dependence of the redox peaks P/P′ for T-PBI and a typical STM image of a high-coverage T-PBI adlayer.

Figure 3(A) illustrates a typical voltammogram of a monolayer of T-PBI in DCM with $TBAPF_6$ as the supporting electrolyte. We identify two pairs of peaks at −0.870 and −1.050 V (versus Ag|AgOx). The peak positions are independent of the scan rate v in 0.01 V $s^{-1} \leqslant v \leqslant 1.00$ V s^{-1}, and their heights scale linearly with v. The total integrated charge of both cathodic (respectively anodic) current peaks amounts, after corrections of the double layer contributions, to 19 ± 1 μC m^{-2}, which corresponds to a coverage $\Gamma = (1.00 \pm 0.08) \times 10^{-10}$ mol cm^{-2}. In consequence, we attribute the two pairs of peaks P2|P2′ and P3|P3′ to the reversible one-electron reduction|oxidation processes of surface-confined T-PBI (T-PBI|T-PBI$^{\cdot -}$; T-PBI$^{\cdot -}$|T-PBI^{2-}).

Qualitatively similar results were also obtained with P-PBI. However, the lower binding affinity of the pyridyl anchor group toward the gold surface caused a partial desorption of the adlayer at $E < -1.00$ V, which prevented a reliable quantitative analysis of reduction peaks and of the corresponding charge density balance. Despite this limitation, we conclude that the reduction potentials of bulk solution and of surface-confined T-PBI (respectively P-PBI) in DCM remain almost the same. We may state that no major alterations of the molecular or electronic structure occurred upon immobilization.

The electrochemical responses of T-PBI and P-PBI adlayers on Au(111)-(1 × 1) in aqueous electrolytes, such as 0.05 M $LiClO_4$ adjusted to pH 12, are somewhat different (figure 3(B)). Both reduction peaks P2|P2′ and P3|P3′ merge into a single broad peak, which we shall label P|P′, with a peak-to-peak separation of 0.070 ± 0.020 V for T-PBI and a slightly larger value of 0.150 ± 0.020 V for P-PBI (figure 3(B)). The peak positions are independent of scan rate v, and their heights scale linearly with v for 0.010 V $s^{-1} \leqslant v \leqslant 1.000$ V s^{-1}. We estimate the formal potentials as $E^0_{\text{T-PBI}} = -(0.790 \pm 0.035)$ V and $E^0_{\text{P-PBI}} = -(0.725 \pm 0.095)$ V. Current integration yields a charge of (20 ± 1) μC cm^{-2} for T-PBI and (20 ± 2) μC cm^{-2} for P-PBI. The corresponding coverages, assuming a two-electron process within a surface-confined adlayer, amount to $\Gamma_{\text{T-PBI}} = (1.03 \pm 0.06) \times 10^{-10}$ mol cm^{-2} and $\Gamma_{\text{P-PBI}} = (1.03 \pm 0.06) \times 10^{-10}$ mol cm^{-2}, which lead to cross-sectional areas of $A_{\text{T-PBI}} = (1.6 \pm 0.1)$ nm^2 and $A_{\text{P-PBI}} = (1.6 \pm 0.2)$ nm^2. Comparing with semi-quantitative modeling using Hyperchem 7.0, we conclude that the cross-sectional area corresponds to a densely packed monolayer of PBI derivatives with their long molecular axis through the two imide nitrogens aligned slightly tilted with respect to the surface normal. A parallel orientation could be ruled out for packing reasons. We also observed that the P-PBI adlayers are less stable at negative potentials, which is attributed to a partial desorption.

The differences in the voltammetric behavior in DCM and an aqueous electrolyte are related to specific solvent–PBI interactions as well as to the possibility of incorporation of cations of the supporting electrolyte, specifically Li^+, into the charged PBI adlayers. The specific role of interfacial water is obvious when starting with a completely dry solution of DCM and than saturating it with water, which leads to a significantly smaller separation between the two reduction peaks.

3.3. Single molecule junction conductance

Employing a modified STM-based break junction technique [52] we recorded i_T–Δz traces of formation and breaking of Au|P-PBI(T-PBI)|Au nanojunctions in aqueous electrolyte under strict potential control and in the absence of oxygen. Comparable *in situ* experiments in a polar organic solvents still failed due to a lack of long-stability of the tip coating material.

Initial experiments revealed high quality voltammograms in the chosen STM configuration, similar to those displayed in figure 3(B) for T-PBI in a large electrochemical cell. In an attempt to minimize intermolecular interactions in our single junction studies, we reduced the surface coverage of the PBI derivatives to 10% up to a maximum 20% of a full monolayer. As a consequence, we obtained a larger number of type I i_T–Δz traces (70%), which indicate that no molecular junctions were formed. The number of noisy curves (type II, 15%) was sufficiently small, and the remaining 15% of type III curves were chosen to construct conductance histograms. The

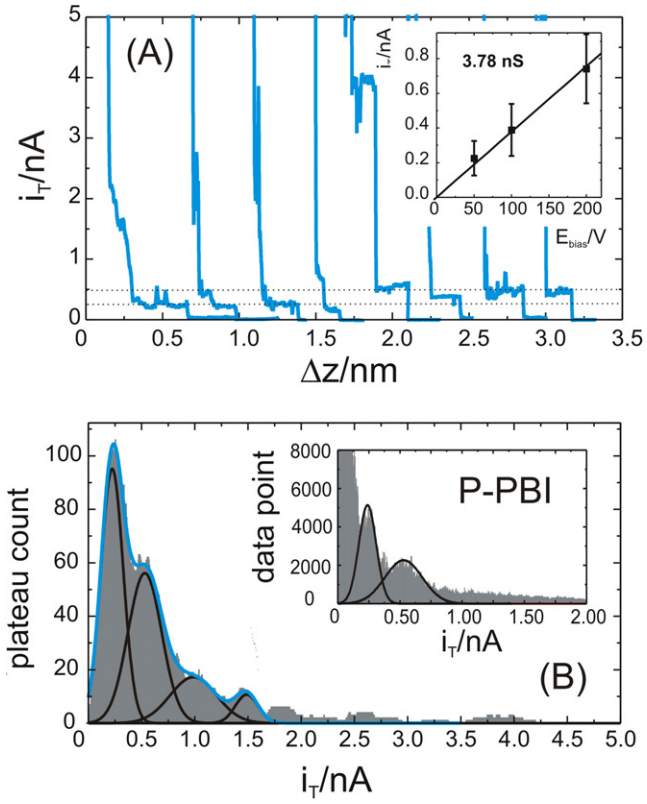

Figure 4. (A) Typical current–distance (i–Δz) retraction curves for P-PBI molecules immobilized on Au(111)-(1 × 1) in 50 mM $LiClO_4$, pH ∼ 12, at $E_{bias} = 0.05$ V; $E_S = -0.12$ V (versus SCE). The inset shows a linear dependence of the conductance current (obtained from statistical analysis) on the bias voltages. (B) Plateau-counting conductance histograms constructed from type III current–distance curves of P-PBI, 250 type III out of 2500 recorded traces; 5 pA bin size. The inset shows the corresponding data-point conductance histograms constructed from the same sets of single traces. The peak positions were determined by Gaussian fits.

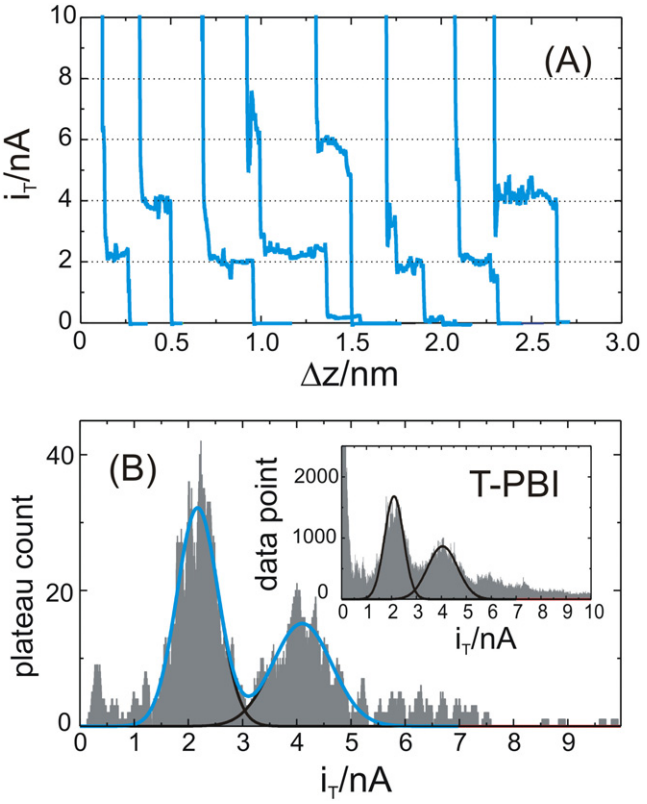

Figure 5. (A) Current–distance (i–Δz) retraction curves for T-PBI molecules immobilized on Au(111)-(1 × 1) in 50 mM $LiClO_4$, pH ∼ 12, at $E_{bias} = 0.05$ V; $E_S = -0.82$ V (versus SCE). (B) Plateau-counting conductance histograms constructed from type III current–distance curves of T-PBI, 140 type III out of 2000 recorded traces; 50 pA bin size. The inset shows the corresponding data-point conductance histograms constructed from the same sets of single traces. The peak positions were determined by Gaussian fits.

occurrence of i_T–Δz traces with clear-cut steps and plateaus was slightly higher for P-PBI than for T-PBI. Figures 4(A) and 5(A) show characteristic i_T–Δz stretching curves for P-PBI at $E_S = -0.120$ V (versus SCE), e.g. within the stability region of the neutral PBI molecule, and for T-PBI at $E_S = -0.820$ V (versus SCE), e.g. within the stability region of the dianion. The bias voltage was adjusted to 0.050 V, and no PBI derivatives were present in solution.

The statistical analysis of individual type III i_T–Δz conductance traces was carried out by constructing plateau-counting (figures 4(B) and 5(B)) and all-data-point histograms (insets in figures 4(B) and 5(B)). Both sets of graphs show a characteristic series of equally spaced current peaks. Compared to our recent study with alkanedithiols, only one single sequence of peaks was observed, indicating a uniform (or not distinguishable) coordination geometry of the anchoring groups. The first current peak of each sequence is attributed to the conductance current of a single molecular junction. The peak position scales linearly with the applied bias voltage in $|E_{bias}| \leqslant 0.20$ V. The particular data sets plotted in figures 4 and 5 for illustration led to single junction conductances of P-PBI at −0.120 V of 3.6 ± 1.2 nS and for T-PBI at −0.820 V of 21.7 ± 3.8 nS. The average values of the junction conductances were estimated from Gaussian fits of up to three consecutive current peaks. The errors were determined by the full width at half-maximum.

The statistical analysis of the plateau lengths, e.g. the stretching distances before breaking a Au|PBI|Au junction, with a pulling rate of 4–8 nm s^{-1}, leads to 0.15 ± 0.10 nm for both molecules, T-PBI and P-PBI. No significant fine structure could be extracted. The experimentally observed stretching distances are identical to 0.10–0.20 nm, which are typical values reported for Au–Au nanocontacts [74], indicating that the breakdown of the junctions most likely takes place at Au–Au bonds.

The widths of the current peaks as well as the plateau length distributions are rather broad, which reflect variations in the microscopic junction, such as metal electrode–molecule contact geometry or molecular conformation [3, 51, 52]. We also note that the two PBI derivatives studied in this work exhibit a twisted or distorted π-system due to the repulsive interactions between the 4-*tert*-butyl-phenoxy substituents. The twisting angle of the PBI backbone and the orientation of the 4-*tert*-butyl-phenoxy groups modify the optical properties of the PBI center [53, 54]. One may expect a similar influence on the molecular conductance.

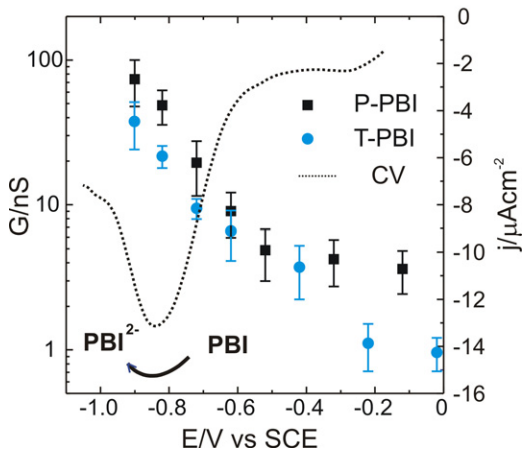

Figure 6. Average conductance values of single molecular junctions *versus* the substrate potential E. The conductance values were determined by Gaussian fits from the first peak positions in the conductance histograms. The error bars represent the widths at half-maximum values of the first conductance peak in the respective histograms. The dashed line corresponds to the single scan voltammogram recorded for a monolayer of immobilized T-PBI on Au(111)-(1 × 1) in 0.05 M $LiClO_4$, pH ∼ 12, scan rate 0.1 V s^{-1}.

The *potential dependence* of the Au|P-PBI(T-PBI)|Au single junction conductance was obtained by repeating the measurements outlined above at variable substrate (E_S) and tip (E_T) potentials, while keeping the bias voltage constant. Three sets of data were recorded at $E_{bias} = 0.050$, 0.100 and 0.200 V for $-0.900\ V \leqslant E_S \leqslant 0.00$ V. The acquisition of data at more negative potentials was hampered by the instability of the PBI adlayers. The probability of forming molecular junctions at more negative potentials decreased considerably compared to in the stability regions of the uncharged molecule. We attribute this trend to the weakening of the Au–Au bond at more negative charge densities, e.g. closer to the potentials of reductive desorption of the pyridine (or thiol) moiety.

Figure 6 shows semilogarithmic plots of the single junction conductances Au|P-PBI(T-PBI)|Au versus the substrate potential E_S. The conductances of P-PBI junctions are typically, e.g. within the entire potential range studied, a factor of 3 larger than for T-PBI. We also observed that the conductances of both systems are rather independent of the electrode potential in the stability range of the neutral PBI species. Decreasing the substrate and tip potentials toward negative values, and approaching the potential regions of the reduction processes P-PBI|P-PBI$^{\cdot-}$ (respectively P-PBI$^{\cdot-}$|P-PBI^{2-}) (and analogously for T-PBI) leads to a rapid increase of the junction conductance up to two orders of magnitude. No plateau or peak was observed at $E \geqslant -0.800$ V. This could be an intrinsic property of the system studied due to a 'soft-gating' mechanism involving conformational dynamics [39]. However, the PBI-based junctions exhibit a rather rigid z-axis, and the only conformational degrees of freedom are introduced by the bulky 4-*tert*-butyl-phenoxy groups at the bay positions. These substituents lead to a propeller-like twisting angle of 22° between the two naphthalene half units [53–55] and prevent π–π stacking of neighboring molecules, or in other words the formation of molecular junction dimers. Both properties may explain the lower conductances of the T-PBI and P-PBI single molecule junctions compared to those reported for the unsubstituted parent molecules [33, 47]. However, the absence of a current plateau or of a maximum $E < -0.800$ V is rather attributed to a lack of reliable experimental data due to instabilities of the adlayer and the onset of desorption. Both processes cannot be neglected because the acquisition of a sufficiently large set of experimental stretching curves (2000–3000) requires a time of 0.5–2.0 h at fixed tip and sample polarization.

In order to better understand the strong gating dependence of the molecular conductance, we have performed a comprehensive transport calculation [71]. Conductances have been obtained within the non-equilibrium Green's function (NEGF) approach as implemented in a home-made simulation package [70, 71][6]. Further technicalities and details of the *ab initio* transport calculations will be reported in a forthcoming theory paper [72]. There we summarize the results, thereby formulating the theoretical picture of the transport process [72]. The current flow is mediated by the LUMO which acquires a finite lifetime, h/Γ (Γ: level broadening), through a small hybridization with the orbitals of the leads as is illustrated in figure 7.

Since the experiment is working in the regime of large voltages, $V \gg \Gamma/e$, one has for the current $I = \pi\Gamma/e$ in units of $2e^2/h$. Our (preliminary) theoretical estimates for the junctions depicted in figure 7 yield a ratio $\Gamma_{P\text{-}PBI}/\Gamma_{T\text{-}PBI} \approx 10$, so that the current flow is strongly enhanced when the thiol coupling (figure 7, right) is replaced by a pyridine coupling (figure 7, left). Note, however, that the amplification ratio $\Gamma_{P\text{-}PBI}/\Gamma_{T\text{-}PBI}$ is very sensitive to the details of the molecule-to-electrode coupling (S–Au, S–Au_2, etc), so that experimental results may substantially deviate from our calculation. Therefore, the theoretical result should be considered as qualitative. To better understand this, we offer the following rationale: all current flow is through the π-orbitals of the connecting pyridyl/phenyl unit. The LUMO hybridization is controlled entirely by how this π-system is connected to the electrodes. With the pyridine coupling there is a direct overlap with the Au-surface states, while in the case of a thiol coupling a mediating S atom has been introduced. Since S levels mix with the benzene π-orbitals only at energies more than 0.5 eV below the Fermi energy, the S atom constitutes a barrier for the current flow through the LUMO which expresses itself as a reduced width $\Gamma_{T\text{-}PBI}$. Our theoretical results compare reasonably well on a qualitative level with the experimental values of $\Gamma_{P\text{-}PBI} \approx 2.1 \times 10^{-5}$ eV and $\Gamma_{T\text{-}PBI} \approx 0.8 \times 10^{-5}$ eV implying $\Gamma_{P\text{-}PBI}/\Gamma_{T\text{-}PBI} \approx 2.6$. (We assume spin-degenerate transport, $U \ll V$.)

In addition to the mentioned microscopic uncertainty, two more conceivable sources for quantitative discrepancies should

[6] We describe the interaction between the 'extended molecule' and the rest of the semi-infinite electrodes via an efficient approximation of the self-energy, represented by a local leakage function, $\sum(r, r') \sim i\eta\delta(r - r')$. To improve convergence with the number of Au contact atoms, we use chaotic contact cavities produced by adding a few adatoms to otherwise symmetric Au pyramids. Then the value of the level broadening η can be varied by one order of magnitude (around ∼0.1 Hartree in the present case) leaving the results for the transmission unchanged to within a few per cent.

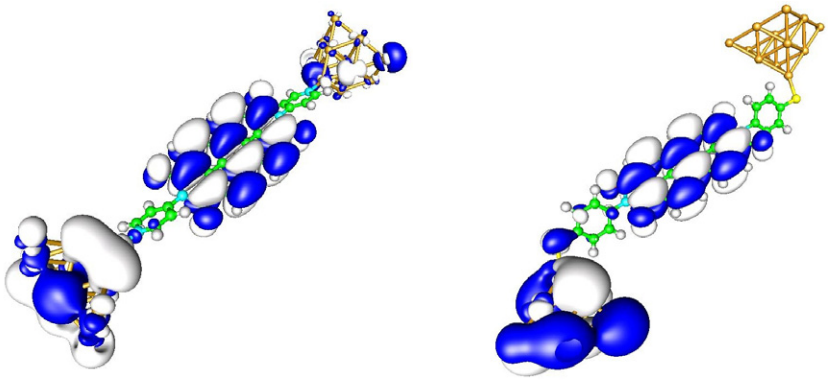

Figure 7. The LUMO of P-PBI (left) and T-PBI (right) molecules on the extended molecule including the perylene units, the pyridine linker groups and two Au_{14} clusters modeling the left and right electrodes. Dark blue/light gray indicate the sign of the wavefunction amplitude. In the case of P-PBI (left) a direct coupling of the pyridine-based N atom to a single Au electrode atom is established. By contrast, the T-PBI molecule (right) is connected via an intermediate S atom.

be discussed: first, theoretical calculations are plagued by artifacts originating from the local density approximation in the exchange functional employed [75]. Second, the *tert*-butyl-phenoxy sidegroups present in the experimental realization have been ignored in our calculations. We believe, however, that the effect of the specific sidegroups that have been employed experimentally in this work is rather weak. These substituents tend to shift the energy of the LUMO slightly and hence the transport resonance, but they do not change its local property. In addition, sidegroups slightly distort the planar geometry of the perylene unit, but again this effect on orbital properties is probably too weak to modify the picture on a qualitative level.

3.4. Asymmetric molecular tunneling junctions

Au(111)-(1 × 1) electrodes covered with a monolayer of T-PBI (or P-PBI), e.g. a disordered high-coverage adlayer, were prepared to create asymmetric tunneling junctions between a bare Au STM tip and a redox-molecule modified adlayer in an aqueous electrolyte. For reference we also measured the tip voltammogram in the absence of tunneling. Typically, the currents did not exceed 5 pA for a scan rate of 1.00 V s^{-1}. The tunneling junction was subsequently formed by letting the tip approach the substrate surface under feedback control until its position was stabilized at a setpoint current $i_T = 100$ pA. Tip and substrate potentials were adjusted in the stability range of the neutral PBI derivative, typically around $E_S = 0.00$ V (versus SCE). Subsequently, the feedback was switched off, and i_T versus E_S (E_T) curves were recorded in the range $-0.35\ \text{V} \leqslant E_S \leqslant -1.200\ \text{V}$ at fixed E_{bias} for 0.5 or 1.0 V s^{-1}. The bias voltage was adjusted between +0.300 and −0.200 V. This approach implies that we changed the Fermi levels of the tip and substrate relative to the redox-active molecular states representing the transition between the neutral PBI derivatives via the radical anion $PBI^{\cdot -}$ toward the di-cation PBI^{2-}.

After each complete negative- and positive-going cycle, the feedback was switched on again, and the system was given sufficient time to stabilize. The coincidence between the initial and the final tunneling current at $E = 0.00$ V

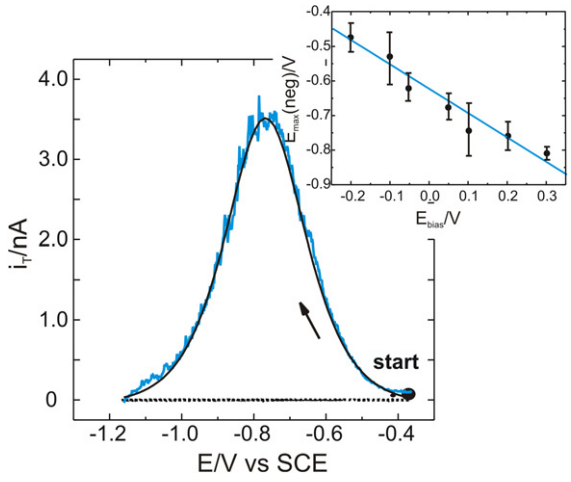

Figure 8. Tunneling current versus substrate potential trace (negative-going sweep) recorded in 50 mM $LiClO_4$ at pH ∼ 12 for a monolayer of T-PBI immobilized on Au(111)-(1 × 1). The bias voltage was fixed to 0.l V. The sweep (1 V s^{-1}) started at $E_S = -0.42$ V, after switching off the tunneling feedback ($i_T = 100$ pA). The blue curve illustrated, as an example, a typical i_T versus $E_{T(S)}$ curve obtained by averaging of 10 independent half-cycles. The solid black line was calculated based on a fit of equation (1) with the following parameters: $\lambda_R = 0.22$ eV; $\gamma = 0.55$; $\xi = 0.38$. The inset shows the bias voltage dependence of the position of the tunneling maximum recorded during negative-going scans.

($i_T = 100$ pA in most cases) and the reasonable agreement between the positive and the negative half-cycle were chosen as criteria for the reliability of the current–voltage traces measured. Figure 8 shows a typical i_T versus E_S tunneling curve for Au|T-PBI|Au constructed by averaging 10 negative-going half-cycles, $E_{bias} = 0.10$ V. The curve exhibits a pronounced maximum at $E_{max}(\text{neg}) = -0.740 \pm 0.075$ V, which is close to the formal potential of the surface-confined molecule, $E^0 = -0.790 \pm 0.075$ V, and does not scale with the scan rate v. The FWHM is estimated as 0.27 ± 0.02 V. The current at the maximum is two orders of magnitude higher than the value at the two turning points $E_S = 0.00$ and

−1.200 V, which represent the stability regions of the neutral T-PBI species or its dianion T-PBI^{2-}, respectively. The large current of the maximum is also significantly higher than the electrochemical background signal (recorded upon retracting the tip in the z-direction out of the tunneling regime) and convincingly demonstrates an enhanced tunneling response modulated by the presence of the redox-active T-PBI molecule. Due to the sharpness of the tip morphology and the exponential distance dependence of the tunneling signal, we assumed that the main contribution to the enhanced tunneling signal in the asymmetric junction originates from a rather small number of redox-active molecules. We also note that the short excursion time to potentials $E < -1.00$ V does not significantly alter the molecular adlayer. This is a distinct advantage over the single molecular stretching experiments described in section 3.3, which require a much longer residence time.

The i_T–E_S characteristics of the positive-going half-cycles exhibit a similar shape, except that the maximum position is localized at $E_{max}(\text{pos}) = -0.640 \pm 0.070$ V, e.g. slightly more positive than E_{max} (neg). This property is intrinsic, and rather independent of the scan rate of the i_T–E_S cycle.

The positions of both maxima depend linearly on the applied bias voltage according to $E_{max}(\text{neg}) = -0.668\ \text{V} - 0.704E_{bias}$ (inset figure 8) and $E_{max}(\text{pos}) = -0.590\ \text{V} - 0.585E_{bias}$. We also notice that the FWHM of the observed tunneling resonances broadens with increasing bias voltage.

A maximum in the tunneling current is predicted by resonance tunneling, a mechanism based on a coherent two-step electron transfer or a sequential two (multi-)step electron transfer process [76–80]. The former two regimes imply a shift of the maximum in the tunneling current by the reorganization Gibbs free energy λ_R with respect to the formal potential. A maximum located close to the formal potential, as observed in the present study, is predicted by the third mechanism. Additional support for this scenario is given by the linear dependence of E_{max} versus E_{bias}. Within the limits of low bias voltages E_{bias} and overvoltages η as well as a sufficiently strong molecule–electrode coupling (adiabatic limit), Ulstrup *et al* proposed the following theoretical formalism [79]:

$$i_T = e\kappa\rho\,(eE_{bias})\,\frac{\omega_{eff}}{4\pi}\exp\left(-\frac{e\,(\lambda_R + E_{bias})}{4k_BT}\right) \times \left\{\cosh\left[\frac{e}{2k_BT}\left(\xi\eta + \left(\gamma - \frac{1}{2}\right)E_{bias}\right)\right]\right\} \quad (1)$$

with

$$i_T(\eta) = i_{T\,max}/\cosh\left[a(\eta - \eta_{max})\right] \quad (2)$$

$$a = e\xi/(2k_BT) = 19.4\xi \quad (3)$$

and

$$\eta_{max} = \frac{1}{\xi}\left(\frac{1}{2} - \gamma\right)E_{bias}. \quad (4)$$

The reorganization free energy λ_R represents the electronic–vibrational coupling, ξ and γ are fractions of the overpotential η and of the bias voltage E_{bias} at the site of the redox center, e the elementary charge, k_B is the Boltzmann constant, and ω_{eff} is a characteristic nuclear vibration frequency; κ and ρ represent the microscopic transmission coefficient and the density of electronic levels in the metal leads, which are assumed to be identical for both the reduction and the oxidation of the intermediate redox group. $I_{T\,max}$ and η_{max} are the current and the overvoltage at the maximum.

The fits of equations (2)–(4) to the experimental curve plotted in figure 8 lead to $\lambda_R = 0.22$ eV, $\xi = 0.38$ and $\gamma = 0.55$. The fits of more than 30 negative- and positive-going half-cycles lead to the average parameters $\lambda_R = 0.17 \pm 0.08$ eV, $\xi = 0.32 \pm 0.08$ and $\gamma = 0.45 \pm 0.15$, indicating a substantial potential drop at the position of the redox site. The value of the reorganization energy λ_R is reasonable and strengthens the proposed mechanism. The good coincidence between the black solid line (calculated curve based on equations (2)–(4)) and the blue trace (experimental result) provides additional support. A detailed analysis of the theoretical formalism expressed by equation (1) will be given in a forthcoming publication [81].

4. Summary and conclusions

We have studied the electron transport characteristics of pyridine- (P-PBI) and thiol-terminated (T-PBI) perylene-3,4:9,10-tetracarboxylic acid bisimides that contain *tert*-butylphenoxy substituents on macroscopic Au(111) single crystal electrodes and in gold nanojunctions.

Voltammetric studies with P-PBI dissolved in DCM reveal two reversible one-electron reduction processes (formation of the stable radical anion PBI$^{\cdot-}$ and of the dianion PBI^{2-}) and one reversible one-electron oxidation (formation of the radical cation PBI$^{\cdot+}$) process. Cyclic voltammetry of immobilized monolayers of T-PBI on Au(111) measured in DCM also reveals two well-defined reduction peaks. In contrast, the electrochemical responses of T-PBI and P-PBI adlayers on Au(111)-(1 × 1) in an aqueous electrolyte show that both reduction peaks merge into a single broad peak. This difference is attributed to specific solvent–PBI interactions as well as to the possibility of incorporating cations of the supporting electrolyte into the charged PBI adlayers.

Employing a custom-designed STM-based break junction technique we recorded i_T–Δz conductance traces of the formation and of breaking of Au|P-PBI(T-PBI)|Au nanojunctions in an aqueous electrochemical environment. We observed that the conductances of both molecular wires are independent of the electrode potential in the stability range of the neutral PBI species. Decreasing the substrate and tip potentials toward negative values, and approaching the potential regions of the reduction processes, lead to a rapid increase of the junction conductance up to two orders of magnitude. These experiments demonstrate that a perylene-based molecular wire can function as a gate-controlled current switch. The conductances of the P-PBI junctions are typically a factor 3 larger than that of T-PBI.

The switching process in symmetric Au|P-PBI(T-PBI)|Au junctions can be understood in analogy to the standard theory of a weakly coupled quantum dot: the current is essentially the sum of the contributions of the number of perylene-based molecular orbitals inside the bias window. We have performed *ab initio* transport calculations which fully support this point of view and which reproduce the experimentally observed current values on a (semi-)quantitative level. Our calculations also suggest that the replacement of the perylene unit by a

'semiconducting quantum dot' might lead to an even higher on/off ratio.

I_T–$E_{S(T)}$ curves of asymmetric molecular junctions formed between a bare Au STM tip and a T-PBI (P-PBI) modified Au(111) electrode in an aqueous electrolyte exhibit a pronounced maximum in the tunneling current at −0.740 V, which is close to the formal potential of the surface-confined molecules. The position of the maximum is linearly dependent on the applied bias voltage E_{bias}. The experimental data were attributed to a sequential two-step electron transfer process. The analysis of a large number of individual traces led to average values of the reorganization free energy $\lambda_R = 0.17 \pm 0.08$ eV and to fractions of the overpotential η and of the bias voltage E_{bias} at the site of the redox center being equal to $\xi = 0.32 \pm 0.08$ and $\gamma = 0.45 \pm 0.15$, respectively. These values are reasonable and strengthen the proposed mechanism.

Acknowledgments

This work was supported by the HGF Project 'Molecular Switches', the SPP 1243, the Volkswagen Foundation and the University of Berne and the Research Center Jülich. IP acknowledges support of the German Academic Exchange Agency for a PhD fellowship. FE, AA and AB acknowledge support from the SPP 1243 'Center for Functional Nanostructures' situated at Karlsruhe University.

References

[1] Aviram A and Ratner M 1974 *Chem. Phys. Lett.* **29** 277
[2] Tao N J 2006 *Nat. Nanotechnol.* **1** 173
[3] Chen F, Hihath J, Huang Z, Liu X and Tao N J 2007 *Annu. Rev. Phys. Chem.* **58** 535
[4] Donhauser Z J, Mantooth B A, Kelly K F, Bumm L A, Monnell J D, Stapleton J J, Price D W, Rawlett A M, Allara D L, Tour J M and Weiss P S 2001 *Science* **292** 2303
[5] Andres R P, Datta S, Janes D B, Kubiak C P and Reifenbeger R 2001 *Handbook of Nanostructured Materials and Nanotechnology* vol 3, ed H S Nalwa (New York: Academic) p 180
[6] Gimzewski J K and Joachim C 1999 *Science* **283** 1683
[7] Lu X, Hipps K W, Wang X D and Mazur U 1996 *J. Am. Chem. Soc.* **118** 7197
Scudiero L, Barlow D E and Hipps K W 2000 *J. Phys. Chem.* B **104** 11899
Scudiero L, Barlow D E, Mazur U and Hipps K W 2001 *J. Am. Chem. Soc.* **123** 4073
Scudiero L, Barlow D E and Hipps K W 2002 *J. Phys. Chem.* B **106** 996
[8] Repp J, Meyer G, Paavilainen S, Olsson F E and Persson M 2006 *Science* **312** 1196
[9] Temirov R, Lassise A, Anders F B and Tautz F S 2008 *Nanotechnology* **19** 065401
[10] Wold D J and Frisbie C D 2001 *J. Am. Chem. Soc.* **123** 5549
Wold D J, Haag R, Rampi M A and Frisbie C D 2002 *J. Phys. Chem.* B **106** 2813
[11] Cui X D, Primak A, Zarate X, Tomfohr J, Sankey O F, Moore A L, Moore T A, Gust D, Harris G and Lindsay S M 2001 *Science* **294** 571
[12] Fan F R, Yang J, Cai L, Price D W, Dirk S M, Kosynkin D V, Yao Y, Rawlett A M, Tour J M and Bard A J 2002 *J. Am. Chem. Soc.* **124** 5550
[13] Xu B and Tao N J 2003 *Science* **301** 1221
[14] Tao N J 1996 *Phys. Rev. Lett.* **76** 4066
[15] Huang Z, Chen F, D'agosta R, Bennett P A, Di Ventra M and Tao N J 2007 *Nat. Nanotechnol.* **2** 698
[16] Seferos D S, Trammell S A, Bazan G C and Kushmerick J G 2005 *Proc. Natl Acad. Sci.* **102** 8821
[17] Reed M A, Zhou C, Muller C J, Burgin T P and Tour J M 1997 *Science* **278** 252
[18] Kergueris C, Bourgoin J P, Palacin S, Esteve D, Urbina C, Magoga M and Joachim C 1999 *Phys. Rev.* B **59** 12505
[19] Reichert J, Ochs R, Beckmann D, Weber H B, Mayor M and v Löhneysen H 2002 *Phys. Rev. Lett.* **88** 176804
[20] Gonzalez M T, Wu S, Huber R, van der Molen S J, Schönenberger C and Calame M 2006 *Nano Lett.* **6** 2238
[21] Lörtscher E, Ciszek J W, Tour J and Riel H 2006 *Small* **2** 973
[22] Park J, Pasupathy A N, Goldsmith J I, Chang C, Yaish Y, Petta J R, Rinkoski M, Sethna J P, Abruna H D, McEuen P L and Ralph D C 2002 *Nature* **417** 722
[23] van der Zant H S J, Osorio E A, Poot M and O'Neil K 2006 *Phys. Status Solidi* b **243** 3408
[24] Chen J, Reed M A, Rawlett A M and Tour J M 1999 *Science* **286** 1550
[25] Tran E, Duati M, Whitesides G M and Rampi M A 2006 *Faraday Discuss.* **131** 197
[26] White H S, Kittlesen G P and Wrighton M S 1984 *J. Am. Chem. Soc.* **106** 5375
[27] Meulenkamp E A 1999 *J. Phys. Chem.* B **103** 7831
[28] Krüger M, Buitelaar M R, Nussbaumer T, Schönenberger C and Forro L 2001 *Appl. Phys. Lett.* **78** 1291
[29] Rosenblatt S, Yaish Y, Park J, Gore J, Sazonova V and McEuen P L 2002 *Nano Lett.* **2** 869
[30] He H X, Zhu J S, Tao N J, Nagahara L A, Amlani I and Tsui R 2001 *J. Am. Chem. Soc.* **123** 7730
He H X, Li X L, Tao N J, Nagahara L A, Amlani I and Tsui R 2003 *Phys. Rev.* B. **68** 045302
[31] Haiss W, van Zalinge H, Higgins S J, Bethell D, Hörbenreich H, Schiffrin D J and Nichols R J 2003 *J. Am. Chem. Soc.* **125** 15294
[32] Alessandrini A, Salerno M, Frabboni S and Facci P 2005 *Appl. Phys. Lett.* **86** 133902
[33] Xu B, Xiao X, Zang X, Yang L and Tao N J 2005 *J. Am. Chem. Soc.* **127** 2386
[34] Chen F, He J, Nuckolis C, Roberts T, Klare J E and Lindsay S M 2005 *Nano Lett.* **5** 503
[35] Albecht T, Guckian A, Ulstrup J and Vos J G 2005 *Nano Lett.* **5** 1451
[36] Li Z, Han B, Meszaros G, Pobelov I, Wandlowski Th, Blaszczyk A and Mayor M 2006 *Faraday Discuss.* **131** 121
[37] Yoshimoto S, Tada A, Suto K, Narita R and Itaya K 2003 *Langmuir* **19** 672
[38] Li Z, Pobelov I, Han B, Wandlowski Th, Blaszczyk A and Mayor M 2007 *Nanotechnology* **18** 044018
[39] Haiss W, Albrecht T, von Zalinge H, Higgins S J, Bethell D, Höbenreich H, Schiffrin D J, Nichols R J, Kuznetsov A M, Zhang J, Chi Q and Ulstrup J 2007 *J. Phys. Chem.* B **111** 6703
[40] He J, Chen F, Lindsay S M and Nuckolls C 2007 *Appl. Phys. Lett.* **90** 072112
[41] Xu B Q, Li X L, Xiao X Y, Sakaguchi H and Tao N J 2005 *Nano Lett.* **5** 1491
[42] Albrecht T, Guckian A, Kuznetsov A M, Vos J G and Ulstrup J 2006 *J. Am. Chem. Soc.* **128** 17132
[43] Albrecht T, Moth-Poulsen K, Christensen J B, Hjelm J, Bjørnholm Th and Ulstrup J 2006 *J. Am. Chem. Soc.* **128** 6574
[44] Xiao X, Nagahara L A, Rawlett A M and Tao N J 2005 *J. Am. Chem. Soc.* **127** 9235
[45] He J, Fu Q, Lindsay S, Ciszek J W and Tour J M 2006 *J. Am. Chem. Soc.* **128** 14828
[46] Xiao X, Brune D, He J, Lindsay S M, Gorman C B and Tao N J 2006 *Chem. Phys.* **326** 138

[47] Li X, Hihath J, Chen F, Masuda T, Zang L and Tao N J 2007 *J. Am. Chem. Soc.* **129** 11535
[48] Chi Q, Farver O and Ulstrup J 2005 *Proc. Natl Acad. Sci.* **102** 16203
[49] Leary E, Higgins S J, van Zalinge H, Haiss W and Nichols R J 2007 *Chem. Commun.* 3939
[50] Chen F, Li X, Hihath J, Huang Z and Tao N J 2006 *J. Am. Chem. Soc.* **128** 15874
[51] Venkataraman L, Park Y S, Whalley A C, Nuckolls C, Hybertsen M S and Steigerwald M L 2007 *Nano Lett.* **7** 502
[52] Li C, Pobelov I, Wandlowski Th, Bagrets A, Arnold A and Evers F 2008 *J. Am. Chem. Soc.* **130** 318
[53] Osswald P, Leusser D, Stalke D and Würthner F 2004 *Angew. Chem. Int. Edn* **44** 250
[54] Osswald P and Würthner F 2007 *J. Am. Chem. Soc.* **129** 14319
[55] Würthner F 2004 *Chem. Commun.* 1564
[56] Grimsdale A C and Müllen K 2005 *Angew. Chem. Int. Edn* **44** 5592
[57] Ranke P, Bleyl I, Simmerer J, Haarer D, Bacher A and Schmidt H W 1997 *Appl. Phys. Lett.* **71** 1332
[58] Dimitrakopoulos C D and Malenfant P R L 2002 *Adv. Mater.* **14** 99
[59] Thelakkat M, Pösch P and Schmidt H W 2001 *Macromolecules* **34** 7441
[60] Ahrens M J, Fuller M J and Wasielewski M R 2003 *Chem. Mater.* **15** 2684
[61] Würthner F, Osswald P, Schmidt R, Kaiser T E, Mansikkamäki H and Könemann M 2006 *Org. Lett.* **8** 3765
[62] Salbeck J, Kunkely H, Langhals H, Saalfrank R W and Daub J 1989 *Chimia* **43** 6
[63] Lee S K, Zu Y, Herrmann A, Geerts Y, Müllen K and Bard A J 1999 *J. Am. Chem. Soc.* **121** 3513
[64] Würthner F, Sautter A, Schmid D and Weber P J A 2001 *Chem. Eur. J.* **7** 894
[65] Baggerman J, Jagesar D C, Vallee R A L, Hofkens J, De Schryver F C, Schelhase F, Vögtle F and Brouwer A M 2007 *Chem. Eur. J.* **13** 1291
[66] Meszaros G, Li C, Pobelov I and Wandlowski Th 2007 *Nanotechnology* **18** 424004
[67] Treutler O and Ahlrichs R 1995 *J. Chem. Phys.* **102** 346
Eichkorn K, Treutler O, Öhm H, Häser M and Ahlrichs R 1995 *Chem. Phys. Lett.* **240** 283
Eichkorn K, Treutler O, Öhm H, Häser M and Ahlrichs R 1995 *Chem. Phys. Lett.* **242** 652
Eichkorn K, Weigend F, Treutler O and Ahlrichs R 1997 *Theor. Chem. Acc.* **97** 119
Sierka M, Hogekamp A and Ahlrichs R 2003 *J. Chem. Phys.* **118** 9136
[68] Becke A D 1988 *Phys. Rev.* A **38** 3098
Perdew J P 1986 *Phys. Rev.* B **33** 8822
[69] Schäfer A, Huber C and Ahlrichs R 1994 *J. Chem. Phys.* **100** 5829
[70] Evers F, Weigend F and Koentopp M 2004 *Phys. Rev.* B **69** 235411
[71] Arnold A, Weigend F and Evers F 2007 *J. Chem. Phys.* **126** 174101
[72] Bagrets A, Evers F and Wandlowski Th 2008 in preparation
[73] Würthner F, Thalacker C, Diele S and Tschierske C 2001 *Chem. Eur. J.* **7** 2245
[74] Xu B Q, Xiao X and Tao N J 2003 *J. Am. Chem. Soc.* **125** 16164
[75] Schmitteckert P and Evers F 2008 *Phys. Rev. Lett.* **100** 086401
[76] Kuznetsov A M and Ulstrup J 2001 *J. Probe Microsc.* **2** 187
[77] Kuznetsov A M and Ulstrup J 2000 *J. Phys. Chem.* A **104** 11531
[78] Schmickler W and Tao N J 1997 *Electrochim. Acta* **42** 2809
[79] Zhang J, Chi Q, Kuznetsov A M, Hansen A G, Wackerbarth H, Christensen H E M, Andersen J E T and Ulstrup J 2002 *J. Phys. Chem.* B **106** 1131
[80] Kuznetsov A M, Medvedev I G and Ulstrup J 2007 *J. Chem. Phys.* **127** 104708
[81] Pobelov I, Li Z and Wandlowski Th 2008 in preparation